AUTHOR(S):

TITLE:

YEAR:

Publisher citation:

OpenAIR citation:

Single Asperity Nanoscratch Behavior of HIPed and Cast

Stellite 6 Alloys

R. Ahmed [*,a,b]**, A. Ashraf** [a]**, M. Elameen** [a]**, N. H. Faisal** [a,c]**, A. M. El-Sherik** [d]**, Y. O. Elakwah** [a]**, M. F. A. Goosen** [e]

[a] *College of Engineering, Alfaisal University, P.O. Box 50927, Riyadh 11533, Saudi Arabia*
[b] *School of Engineering and Physical Sciences, Heriot-Watt University, Edinburgh, EH14 4AS, UK*
[c] *School of Engineering, Robert Gordon University, Garthdee Road, Aberdeen, AB10 7GJ, UK*
[d] *Research & Development Centre, Saudi Aramco, Dhahran, 31311, Saudi Arabia*
[e] *Office of Research & Graduate Studies, Alfaisal University, P.O. Box 50927, Riyadh 11533, Saudi Arabia*

Abstract

The aim of this study was to investigate the nanoscale sliding wear behaviour of re-HIPed (Hot Isostatically Pressed) and cast cobalt-based Stellite 6 alloys. A nanoindentation system equipped with a wear testing module was used to simulate single asperity deformation behaviour using a sphero-conical indenter. The test load was either increased linearly over the sliding distance or ramped up to full load at the initial stage of the test. Post-test evaluations included X-ray diffraction (XRD), scanning electron microscopy (SEM) and atomic force microscopy (AFM) measurements. An elastic-plastic finite element model (FEM) was used to compare the displaced volume with the experimental data. Results are discussed in terms of the structure-property relationships and indicated that the nanoscale wear was dominated by the composition and nanomechanical properties of the metal matrix, and also the shape and size of carbides. Wear predominantly occurred due to plastic deformation of the metal matrix phase. Relatively higher scratch resistance and hardness of the metal matrix phase, coupled with the microstructural homogeneity of re-HIPed alloy led to its lower wear volume loss, in comparison to the cast counterpart. The FEM predictions were in agreement with the experimental results, and the error between the two ranged from 0% to 25% under the loading conditions considered in this investigation.

Keywords: nanotribology; nanoscratch; Stellite alloy; HIPing; nanoindentation; cobalt-based alloys**.**

Research Highlights:

- Metal matrix properties dominate nanoscale wear in Stellite 6 alloys.

- Re-HIPed Stellite 6 alloy performs better than the cast counterpart during nanoscale wear.

- Shear bands were observed in the cast alloy but not in the re-HIPed counterpart during nanoscratch tests.

- Solid solution strengthening and lower stacking fault energy restrict FCC to HCP transformation in re-HIPed alloy.

---

*   Corresponding author R.Ahmed@hw.ac.uk

1. INTRODUCTION

Stellite 6 which has a nominal wt.% composition of Co - 28%Cr - 4.5%W - 1%C, is one of the most widely used cobalt-based alloys for industrial applications [1]. This cobalt-based alloy is generally used in the power generation, marine, automotive, aerospace, and oil and gas industries to provide wear resistant components particularly in lubrication-starved, high temperature, or corrosive environments [2-3]. Despite wide ranging use of this alloy, there is limited published research comparing the nanoscale tribo-mechanical behavior of this particular alloy, produced by the two different manufacturing processes of re-HIPing (Hot Isostatic Pressing) and casting. These changes in manufacturing processes dictate the structure-property relationships and hence their tribo-mechanical behavior. Whilst industrial demands push the use of these alloys to higher stress applications, changes in manufacturing processes can be adapted to produce alloys which can deliver required tribo-mechanical performance.

Benefiting from the FCC (Face Centered Cubic) to HCP (Hexagonal Closely Packed) phase transformation of cobalt, the solid solution strengthening by tungsten, and the formation of hard Cr/W-rich carbides; Stellite 6 alloy has high strength and excellent resistance to abrasive/sliding wear, galling, and high-angle erosion [1]. This alloy is generally used in impact and fatigue resistance applications such as valve seat and gate, pump shaft and bearing, erosion shield, and rolling couples [1]. The structure-property relationships of cast CoCr28W alloy has been a topic of research for a number of investigations [1-5]. The cast alloy exhibits a hypoeutectic microstructure with the primary FCC Co-rich dendrites surrounded by Cr-rich M_7C_3 (M=metal) eutectic carbides. With the addition of molybdenum, silicon or yttrium, $M_{23}C_6$ carbides could also be formed [6-8]. The influence of the content and morphology of carbide on the abrasive wear of cobalt-based alloys has also been a topic of research in published literature [9-15]. For example, various wear mechanisms during the sliding wear tests, such as carbide fracture, carbide pullout, and ploughing on the matrix have previously been reported [16-19].

Investigations relating to the tribo-mechanical comparison of cast and HIPed (Hot Isostatically Pressed) or re-HIPed Stellite 6 alloys are limited in the published literature [20-23]. Re-HIPing is a process of HIPing already HIPed alloy to refine microstructure [22]. These studies have indicated that although carbide refinement due to HIPing leads to improved tribo-mechanical performance in fatigue and fracture resistance [23], the properties of the metal matrix, influencing the structure property relationships, are critical to this improvement. This is consistent with HIPing of surface coatings where microstructural refinement can yield improved tribological performance [24-25]. Furthermore, nanoscratch testing of carbide and metal matrix phases can provide an understanding of the performance of individual microstructural features in both cast and re-HIPed alloys. This understanding at the individual phase level is not appreciable in macro- or micro-scale tribomechanical evaluations [20-21]. Nanoscratch test evaluations therefore provide an understanding of single asperity deformation of engineering materials which can be used for the assessment of wear mechanisms, mathematical and numerical modelling of wear, and other nanoscale experimental investigations such as in-situ wear

measurements in the SEM chamber, and subsurface analysis of a worn surface using focused ion beam (FIB). One such investigation was recently reported by Sebastiani et al. [26], who reported on the wear track of Stellite 6B alloy used for the lip-seal of a tunnel boring machine. They concluded that under such conditions, nanoscale two and three-body abrasion caused by the contaminant in the lubricant oil dominate the wear mechanism. Nanoscratch evaluations of Stellite alloys manufactured via different routes is almost nonexistent in the published literature. Macroscratch testing of hardfacing Stellite alloys is also scarce in the published literature except for the investigation reported by Yao et al. [27], where a scratch load of 20N was used to fracture carbides in macroscale scratch tests. Scratch data was analyzed using the acoustic emission method.

The aim of the current study was to ascertain deformation and cracking behavior at the nanoscale using nanoscratch testing of re-HIPed and cast Stellite 6 alloys. Investigations included Scanning Electron Microscopy (SEM), Energy Dispersive X-ray Spectroscopy (EDS), X-Ray Diffractometry (XRD), nanohardness and nanoscratch wear evaluations. Experimental and Finite Element Model (FEM) results are compared with a view to ascertain the single asperity nanoscale wear behavior of Stellite 6 alloys.

2. EXPERIMENTAL PROCEDURES

2.1. Materials and microstructure

The HIPed alloy was produced by canning the gas-atomized powders at a temperature and pressure of 1200˚C and 100MPa, respectively, for 4 hours in a HIPing vessel. **Table 1** summarizes the chemical compositions of both re-HIPed and cast Stellite 6 alloys. Re-HIPing of the alloy was conducted un-encapsulated under the same conditions, after the first HIP cycle. The sieve analysis of these powders (+250μm (0.1wt.%); -250+180μm (9.3wt.%); -180+125μm (23.8wt.%); -125+45μm (50.3wt.%); -45μm (16.4wt.%)) indicated that 75wt.% of the powder particles were in the size range of 45 to 180 microns. The cast alloy samples were produced via sand casting process. The microstructure of the powders and both alloys was observed via SEM equipped with a Back-scattered Electron Imaging (BEI) detector. The chemical compositions of different phases developed in the powders and alloys were determined via EDS and XRD with Cu-K_α radiation (wavelength = 1.5406Å). Image analysis was also conducted to ascertain the area fractions of individual phases.

2.2. Nanoindentation tests

Nanoindentation testing which included nanohardness and elastic modulus measurements were performed using a calibrated nanoindentation system (NanoTest™ - Micro Materials Limited, UK) equipped with a standard Berkovich nanoindenter tip. Measurements were performed at room temperature (~23°C) in load control mode at a load of 50 mN. The indentation procedures were programmed as three segments of trapezoidal shape with 10 s loading, 5 s hold and 10 s unloading segments. Eighteen equally spaced measurements were performed on the cast alloy sample whereas twenty-five equi-spaced measurements were performed on the re-HIPed alloy. The P-h profiles were analyzed using standard methods with the area function for the Berkovich indenter which was determined by indentations into fused silica with elastic modulus of 69.9 GPa. The raw data (P-h

profile) was used to evaluate the hardness and reduced elastic modulus (Er) using the Oliver and Pharr method [28]. The elastic modulus and Poisson's ratio of the diamond indenter were taken as 1140 GPa and 0.07, respectively. The indentation instrument consisted of an optical microscope and an integrated atomic force microscope (AFM), directly linked by an automated positioning system.

2.3. Nanoscratch sliding wear tests

Nanoscratch (sliding wear) tests were performed with a sphero-conical diamond indenter of 10 μm tip radius and 60° apex angle. This was akin to single asperity abrasive scratch wear of Stellite alloys with a view to understand the role of individual microstructural features dominating the wear and deformation process. The scratch tests were performed as multi-pass tests at sliding velocity of 2 μms^{-1} over a 60 μm track with (a) pre-scratch topographic scan, (b) a leveling distance followed by a ramped scratch, and (c) a post-scratch low load scan. In the pre- scratch and post-scratch scan the applied load was sufficiently low (10 μN) so that no wear occurred, and was used to measure the topography of scratch surface before and after the scratch test. Four different loading conditions were used during the scratch testing as summarized in **Figure 1**. In the 'on-load' scratch scan the load was ramped linearly after 20 μm travel at 2.5 mN/s to reach 50 mN and at 5 mN/s to reach 100 mN for loading conditions 1 and 2, respectively. For the loading conditions 3 and 4, the load was increased linearly after 20 μm travel at 25 mN/s to reach 50 mN and at 50 mN/s to reach 100 mN, respectively.

Six repeat tests were performed to test the reproducibility of the scratch behavior for each of the loading condition shown in Figure 1. The scratches were spaced 25 μm apart and it was expected that the probe would not be deflecting the path when it encounters a large carbide phase in the soft matrix. In terms of energy, which is represented by the area under the force displacement curve for loading conditions 1 to 4 was 1μJ, 2μJ, 1.955 ≈ 2μJ and 3.83μJ, respectively.

Post-scratch test imaging using AFM and SEM was also employed to investigate the residual surface features. Wear volume was calculated by exporting the 3D map of the surface from AFM software (NanoSurf™) in MATLAB®. A computer code was written to calculate the volume below and above the mean plane using the trapezoidal rule representing scratch volume and pile-up volume, respectively. The computer code applied the routine of calculating the wear volume automatically using the mean plane to each row of 3D surface data in MATLAB®.

2.4. Finite element modeling of scratch test

The nanoscratch scenario was modeled as an elastic-plastic contact model implemented in a commercial FEM platform of ANSYS (R14). In this study, a spherical indenter (diamond) comes in contact and slides with a ramping force on the surface of the Stellite 6 alloy, which is assumed to display an elasto-plastic behavior [29]. Material properties used in the current analysis for re-HIPed and cast Stellite 6 alloys are shown in **Table 2**. The indenter was modeled as rigid with a tip radius of 10 μm. **Figure 2** shows the model with a grid in 3D. The mesh follows an element size of 1 μm to keep balance of accuracy and computation time. The model consisted of 49,665 elements of the type CONTA171 and TARGEI69. The scratch and loading dimensions were in accordance with the experimental set-up for each loading condition as summarized in Figure 1.

4

3. RESULTS

3.1. Microstructure and phase analysis

Figures 3 and **4** provide the SEM and XRD comparison of the cast and re-HIPed alloys. Figure 3a shows the SEM of the dendritic microstructure on the spherical surface of the gas atomized powder. Figure 3b and 3c show the hypoeutectic microstructure of the cast alloy, which consisted of Cr-rich carbides (dark phase), W-rich carbides (bright phase), and the Co-rich dendritic matrix (grey region). Figure 3d shows the SEM observation of the re-HIPed alloy, with finer carbides (dark phase) uniformly distributed in a Co-rich matrix (grey region). The image analysis results of the area fractions of various phases are presented in Table 3, which represents an average of five measurements for each alloy.

3.2. Nanohardness and modulus

Figures 5 and **6** indicate the location of nano-indentations on the cast and re-HIPed alloys. Inserts within the light microscope images indicate SEM observations of the indents which landed in the metal matrix and carbide phase. The average nanohardness and modulus measurements of the cast and re-HIPed Stellite 6 alloys are summarised in **Table 4**. This Table also shows the maximum and minimum values relating to hardness and modulus of carbide and metal matrix phases to aid the discussion. However, these values are only indicative as the measurements on the matrix and carbide phase can be influenced by the neighbouring and underlying material as will be discussed later. Previously reported microhardness and macrohardness values are also reported in Table 4 to aid the discussion [22-23].

3.3. Nanoscratch testing

The AFM, SEM and topography imaging was conducted for all scratches considered in this investigation. **Figure 7** shows typical scratch observation comparisons for loading conditions 1 and 3. **Figure 8** shows the AFM, scratch and post-scratch topography scans along the length of the scratch, and SEM observations for loading condition 2. The scratch scan indicates the displacement of the indenter tip during a scratch, whereas the post-scratch scan indicates the topography of the groove after the scratch test. The difference between the scratch and post-scratch scans indicate the extent of elastic recovery after unloading.

Figure 9 shows the AFM, scratch and post-scratch topography scans and SEM observations for loading condition 3. **Figure 10** shows the averaged profile of all six post-nanoscratch wear scar depths along the scratch axis for all four loading conditions considered in this investigation. The average wear scar depths shown in Figure 10 ranged from 100nm to 300nm for the loading conditions considered in this study. They were shallower than the indentation depths measured in nanohardness measurements which ranged from 440 nm to 625nm. The displaced average wear volume during scratch testing evaluated using the MATLAB® code for all loading conditions is summarised in **Figure 11**.

3.4. Finite element modelling of scratch

The FEM described earlier in section 2.4 was solved in successive displacement iterations for the loading conditions summarised in Figure 1. **Figure 12**, shows the actual and modelled scratches for ramping load of 100mN (loading condition 2). To further verify the accuracy of the model, the volume displaced by both scratches was compared. The volume displaced in FEM was calculated by difference of the base volume under x-z plane before and after the scratch. The indenter causes a plastic flow of the material on both sides of the scratch. The edge built-up is therefore above the x-z plane corresponds to volume removed from the scratch, due to volume conservation, as observed in Figure 12. **The** results of wear volume for all load cases are summarised in **Figure 11.**

Figure 13 shows the contour of cumulative Von Mises stress after the wear scar stroke along the thickness (y-axis). Figure 13a shows the contour of cumulative Von Mises stress after the wear scar stroke along the thickness (y-axis). Figure 13b represents the stress distribution laterally (z-x axis). There is build-up of material towards the end of stroke which is consistent with the experimental observations.

4. DISCUSSION

4.1 Microstructure Examination

The cast Stellite 6 alloy had a hypoeutectic microstructure (Figures 3b, c), which consisted of Co-rich dendrites (grey region), set in lamellar eutectic Cr-rich (dark phase) and W-rich (bright phase) carbides. The Cr-rich eutectic carbide had a composition of $(Cr_{0.71}Co_{0.25}W_{0.03}Fe_{0.005})7C_3$, as approximated by the EDS analysis. The XRD analysis (Figure 4c) of cast alloy revealed that the carbides were Cr_7C_3 and Co_6W_6C, whilst α-Co (FCC) was the primary phase in the solid solution, together with the inter-metallic compounds, Co_3W and Co_7W_6. This dendritic microstructure is typical of cast CoCr28W alloy in which carbide and grain size can be controlled by the rate of cooling.

Within the family of the cast cobalt-based alloys, the relatively large carbide size seen in the cast microstructure indicated slow freezing during the casting process. The microstructure of cast Stellite 6 alloys have been a topic of research for a number of investigations and further details of the influence of cooling rate on the grain size of cast cobalt-based alloys can be appreciated elsewhere [13]. The scope of the discussion here is therefore its microstructural comparison with the re-HIPed counterpart in terms of understanding the nanoscale structure-property relationships during tribo-mechanical performance.

The re-HIPed alloy had a much finer microstructure (Figure 3d) with Cr-rich carbides (dark phase) uniformly distributed in the matrix. The typical carbide size was 1-3μm, which was much finer than that of the cast counterpart. There was no bright (W-rich) phase observed in the re-HIPed microstructure, which could be attributed to the fast solidification in the powder manufacture process, restricting the segregation of W-rich zones. During re-HIPing, tungsten remained evenly distributed throughout the alloy matrix, because its relatively larger atomic radius hinders diffusion. This distribution of tungsten in metal matrix phase influences the nanoscale tribo-mechanical performance of re-HIPed alloy in comparison to the cast counterpart, as the high area fraction of metal matrix (85%) in both cast and re-HIPed alloys dominates the microstructure (Table 3). The evolution of re-HIPed microstructure was therefore fundamentally different from the dendritic microstructure of the cast alloy.

6

This difference was caused by the rejection of elemental species in the melt during crystal growth of Co-rich dendrites in the cast alloy. Hence above the liquidus line of this complex Co alloy, elemental species were free to arrange themselves depending upon the thermal kinetics of the mould without any dependency on diffusion, and hence a truly three dimensional network of carbides was formed. Contrary to this, in the case of re-HIPed microstructure, primary dendrites formed on the alloy powder (Figure 3a), and the carbides in the powder particles (Figure 4a) promoted carbide growth due to diffusion of carbon and other elemental species within and across the individual powder particle boundaries. As this diffusion process was time, temperature, and pressure dependent during HIPing, and the HIPing temperature (1200°C) was lower than the melting point of the powder, carbide growth was sluggish when compared to the casting process. Hence the size of individual carbide particles was much finer than that of the cast counterpart.

The XRD analysis (Figure 4b) revealed that the possible phases in the re-HIPed alloy were Cr_7C_3, α-Co, Co_3W, and Co_7W_6, which were similar to those in the cast alloy, except for the absence of Co_6W_6C. The inter-metallic compound, Co_7W_6, was not identified in the atomised powder, indicating it was formed during the re-HIPing process. The pure Cr phase in the powder, which formed due to the rapid solidification, was not identified in the re-HIPed alloy, indicating that it either was combined with cobalt, or formed carbides. The image analysis (Table 3) results showed that the cast alloy had an approximate total carbide fraction of 15.5%, which was similar to the re-HIPed alloy (15%). These differences in the microstructure, carbide shape and morphology influence the nanoscale structure property evaluations as discussed in the next sections.

4.2 *Nanohardness and modulus analysis*

The average values of nanohardness and modulus provided an overall assessment of elastic-plastic response of re-HIPed and cast Stellite 6 alloys at nanoscale. The average values were dominated by the indentations on the softer metal matrix which comprised almost 85% of the surface area of alloy as indicated by the image analysis results (Table 3). However the difference in the hardness of carbides and metal matrix, where the hardness of carbides was much higher (16 to 14.9 GPa for cast alloy) in comparison to 6.4 to 6.9 GPa for the metal matrix, compensated for the difference in area fractions. Hence the averaged nanohardness values in Table 4 represent an overall response of the individual microstructural phases for both alloys. The averaged nanohardness of the re-HIPed alloy was slightly higher than the cast counterpart, albeit higher standard deviation of the hardness of cast alloy. This difference in values between the HIPed and cast alloys is consistent with previously reported hardness measurements at micro- and nano-scales for HIPed Stellite 6 and Stellite 20 alloys [22,23], which showed that not only microstructural variations but also indentation size effects influence the measured average values.

The carbide hardness of the cast Stellite 6 alloy (16 ~ 14.9 GPa - Table 4) was much higher than the re-HIPed counterpart (11.5 to 10.5 GPa). This was partly due to the presence of W-rich carbides in the cast alloy (Figures 3c and 9h), and partly due to the finer carbide size of the re-HIPed alloy (1~3 µm) in relation to the size of nanoindentation (< 3 µm), as shown in Figures 5 and 6. This finer carbide size indicates that carbide hardness for the re-HIPed alloy will be more significantly

influenced by the neighbouring and underlying material in comparison to the cast counterpart. The metal matrix of the re-HIPed alloy however showed higher hardness (7.4 ~ 7.9 GPa) in comparison to the matrix hardness of the cast alloy (6.4 ~ 6.9 GPa). This was due to a higher proportion of retained tungsten in the metal matrix of the re-HIPed alloy providing solid solution strengthening as discussed earlier in section 4.1. Hence based on the hardness values, the metal matrix in the re-HIPed alloy is expected to provide more resistance to abrasive wear during single asperity nanoscratch tests.

The percentage difference in average modulus values was not as substantial (Table 4) as hardness except for the carbide modulus. These differences in modulus values reflect the changes in the bonding strength within the carbides and metal matrix. The differences in modulus and hardness of individual microstructural phases in the two alloys is expected to influence the ratio of elastic plastic work during nanoscratch testing, as discussed in the next section.

4.3 *Nanoscratch tests*

The nanoscratch test methodology enabled the evaluation of nanoscale differences in the wear behaviour of metal matrix and carbide phases. The nanoscratch and cyclic nanoindentation tests are one of the most widely used effective methods for obtaining the critical loads that are related to adhesion properties of thin films and coatings [30-31]. A recent investigation by Jeng et al. [32] considered the influence of grain size and orientation on the tribo-mechanical properties of nickel films using nano-indentation, nano-scratch and nano-wear tests. This investigation concluded that plane orientation with stronger binding energy results in relatively improved tribo-mechanical performance. However, in the current investigation this has been used to investigate the scratch properties of an alloy i.e. ploughing through the carbide and metal matrix phase. During scratch testing, material failure can occur by tensile stress behind the probe (through-depth cracking) and also due to compressive stress, as the hard carbide can separate from the metal matrix phase either by cracking and lifting (buckling) or by full separation (chipping). Furthermore, in the present investigation the behaviour in the cast alloy was predominantly plastic (Figures 8f, 8h and 9f, 9h) with no fracture, whereas an observation of carbide fracture was seen in the re-HIPed alloy (Figure 8g).

4.3.1 *Carbide response during nanoscratch testing*

Chipping was not observed in the current investigation. Carbide fracture in the re-HIPed alloy, with the exception of Figure 8g, was not a common feature under the loading conditions considered in this investigation. Typical brittle tensile cracking, e.g. nested micro-cracks in the direction of scratch but appearing behind the probe due to tensile stress was not observed, and Hertzian cracking, e.g. series of nested micro-cracks within the scratched path was also not detected. Plastic flow of metal matrix resulting in lack of carbide support could be one of the main reasons for fracture of carbides (e.g. for the case of re-HIPed alloy in Figure 8g). The carbide fracture (e.g. Figure 8g) can also be related to buckling and wedging action ahead of the probe tip.

Carbides in the cast alloy also did not show appreciable wear, deformation or fracture. Hence the nanoscratch response was dominated by the properties of the metal matrix phase. This is highlighted in Figures 8(d, f, h), which compares the high magnification SEM morphology and post-

scratch wear depth profile. The post-scratch profile between the 20µm and approximately 35µm sliding distance in Figure 8d shows maximum deformation of approximately 6nm, which can be considered negligible in comparison to the overall deformation of 290nm at the end of the scratch. This part of the scratch relates to the period when the nanoindenter scratched over the carbide phase as shown in the SEM observation in Figures 8f and 8h. Further flattening of depth curve in Figure 8d was also observed between the scratch distance of approximately 42 µm to 50 µm due to a comparable effect. A similar association could be made from Figure 9 (d, f, h), where the post-scratch profile between the 25µm and approximately 35µm sliding distance in Figure 9d showed decrease in contact depth under constant load condition due to carbide interaction as nanoindenter scratched over the carbide phase as shown in the SEM observation in Figures 9f and 9h.

4.3.2   *Metal matrix phase during nanoscratch testing*

In contrast to the response of carbides, the metal matrix phase in the cast alloy plastically deformed with lower nanoscratch resistance in comparison to the re-HIPed alloy, resulting in the formation of shear bands as marked by the white arrows in Figures 8f and 9(f,h). Shear bands were not observed in the re-HIPed alloy. The formation of shear bands during nanoscratch testing in other materials, such as metallic glasses, amorphous alloys and forged Al6061 alloy, have previously been reported in published literature [33-35]. Stellite 6 due to high cobalt content is known to strain harden considerably and undergo strain dependent phase transformation [1-4]. The presence of shear bands in the cast alloy indicated a higher work-hardening rate and a higher tendency of strain induced phase transformation.

Klarstrom et al. [5] has indicated that alloying elements such as iron, manganese, nickel, and carbon tend to stabilize the FCC structure and increase stacking fault energy (SFE), whereas elements such as chromium, molybdenum, tungsten, and silicon tend to stabilize the HCP structure and decrease SFE. The FCC to HCP transformation reaction is quite sluggish even for pure cobalt. However, in metastable compositions, it can be promoted by cold work via a mechanism involving the coalescence of stacking faults. This phenomenon provides a practical limit in the design of wrought cobalt-based alloys in terms of the manufacturing methods that can be used to produce various product forms. The FCC structure has many slip systems for dislocations to cross slip onto, hence implying a low work hardening rate. However, the SFE of Co is relatively low, about only 15-50mJ/m^2 (e.g. the SFE of Ni is 128mJ/m^2), which makes the dislocations to easily dissociate into partial dislocations separated by an area of stacking fault. The mobility of dislocation is thus restricted, and cross slip hardly occurs. Therefore the low SFE hinders the cross slip movement of dislocations and the interactions between these partial dislocations result in rapid work hardening, which will be higher in the metal matrix phase of cast alloy Stellite 6 alloy due to the increase in dislocation density, caused by its relatively lower hardness and hence lower yield strength in comparison to the re-HIPed counterpart. Hence, higher tungsten content in the solid solution of re-HIPed Stellite 6 alloy indicates a decrease in the SFE, resulting in wider stacking faults which makes cross-slip and climb difficult. However in the case of cast alloy, due to relatively higher SFE caused by the absence or lower content of tungsten in the metal matrix phase, dislocation is easier via edge dislocation. Similarly, the presence of a higher tungsten

content in the metal matrix of re-HIPed alloy will roughen the slip planes making dislocation flow difficult. Both of these factors, along with the relatively higher hardness metal matrix in the re-HIPed Stellite 6 alloy, and coarse carbide structure in the cast alloy providing inadequate support to parts of the metal matrix, resulted in lower average volume loss (Figure 11) and lower average wear scar depths (Figure 10) of the re-HIPed alloy.

The FCC to HCP transformation in cobalt-based alloys is not a phenomenon limited to nanoscale deformations e.g. Persson et al. [36] investigated the room temperature self-mated highly loaded dry sliding performance of Stellite 21 and concluded that during high load dry sliding, a Co-enriched tribofilm is created which exhibits low friction and high galling resistance. The tribofilm evolved via FCC to HCP phase transformation under strain. The martensitic transformation of Co from FCC to HCP also strengthens the alloy when it happens. The HCP structure has only one slip plane, indicating that it has limited dislocation mobility and high work hardening rates. However, for high carbon Stellite alloys such as Stellite 20, the influence of work hardening in the matrix on the mechanical properties and wear resistance is usually overshadowed by the contribution of carbides. Although the current investigation deals with nanoscale measurements, unlike the highly loaded sliding considered by Persson et al. [36], the mechanism of martensitic transformation is similar leading to the formation of shear bands.

For the case of re-HIPed alloy the wear scratch constituted ploughing through the carbide and metal matrix phase. Although the overall area fraction of carbides in re-HIPed alloy was similar to the cast counterpart, the size and shape morphology was fundamentally different as the re-HIPed alloy had two-dimensional finer carbides as opposed to the three-dimensional interdendritic network of the cast counterpart. However as the scratch load was low, these smaller carbides resisted ploughing throughout the wear track (Figures 8(e, g) and 9(e, g)) and hence resulted in slightly lower volume loss for the re-HIPed alloy (Figure 11). The uniformity of the re-HIPed microstructure also resulted in a lower standard deviation of the volume loss results when compared to the cast counterpart, for all loading conditions considered in this investigation.

4.3.3 *Influence elastic-plastic ratio*

The difference in areas under the scratch and post-scratch curves in Figures 8c,d and 9c,d, also referred to as degree of wear, can provide relative changes in the elastic recovery of material after the removal of scratch load. For all loading conditions considered in this investigation, the averaged areas under the elastic-plastic curve during scratch, and residual plastic work in the post-scratch depth profiles, was calculated using the trapezoidal rule. These areas were used to calculate the relative differences in the ratio of elastic to plastic and also elastic to elastic-plastic energy. Although the area under the scratch and post-scratch curves in Figures 8c,d and 9c,d do not provide a direct measure of energy as y-axis is scratch depth not force, however it is appreciated that the scratch depth is a function of the scratch force. Hence, the areas under the curve can be used to comprehend relative changes in the energy absorbed during elastic and plastic work e.g. the average areas under the scratch curves for loading conditions 1 to 4 were calculated as 6, 10.5, 10.5 and 18 μm^2, respectively. These areas compare well with the input energy for loading conditions 1 to 4 of 1, 2, 2 and 4 μJ, respectively (Figure 1). Hence a

calibration function can be used to quantitatively relate the area under the scratch and post-scratch curves with energy. As the current analysis concerns relative changes in the measured property of the two alloys, the area under the curves can be directly used for the relative comparison without a calibration function.

The relative changes in elastic plastic energy can thus be evaluated using the areas under the scratch and post-scratch curves. This analysis is presented in in Figure 14, which indicates the extent of relative elastic energy recovery for all loading conditions. This was computed using the percentage ratio $\{(Area_{scratch} - Area_{post-scratch})/ (Area_{scratch})\}$ of the difference in the area under the scratch $(Area_{scratch})$ and post-scratch $-(Area_{post-scratch})$ curves. The recovery ratio was higher for the re-HIPed alloy in comparison to the cast counterpart indicating that the relative energy consumed in the elastic deformation was higher for the re-HIPed alloy. This is consistent with slightly higher averaged reduced elastic modulus of re-HIPed alloy (Table 4). The magnitude of this difference diminishes with the increase in input energy (Figure 1) as the proportion of plastic work increases. The difference in the elastic recovery between the two alloys was dependent on the bond strength within and across the microstructural phases.

4.3.4   Influence of loading condition

Tribological test conditions during the nanoscratch testing also had an effect on the wear volume. This can be understood by comparing the wear volume of loading conditions 2 and 3 in Figure 11. The total average energy of loading condition 2 and 3 was 2 μJ (Figure 1). However their wear performance is different which is attributed to the differences caused by the ramped and constant load conditions. Although the energy is the same for loading conditions 2 and 3, the maximum load is higher for loading condition 2 indicating the influence of higher strain rate in loading condition 2 leading to higher wear volume.

4.3.5   Implications for lubricated contacts

Although the investigations above relate to dry sliding of nanoprobe on the Stellite alloys, the mechanism of improvement in wear performance of the re-HIPed alloy is related to the properties of the metal matrix phase, which has implications on wear and deformation behaviour in lubricated tribological contacts. During process such as rolling and drawing, the lubricant has the tendency of entrapping in surface features, leading to the deformation mechanism of micro-plasto hydrodynamic lubrication (MPHL). Details of MPHL in cold rolling and strip drawing of steels can be appreciated in earlier publications [37, 38]. Implication of the nanoscratch work presented here indicates that the MPHL behaviour in manufacturing processes such as rolling and drawing for the re-HIPed and cast Stellite 6 alloys will be different due to the microstructural and nanoscale tribo-mechanical differences in the metal matrix phase. Of course, the carbide size and shape will also influence the overall rolling or drawing deformation, but the emphasis here is MPHL, which is known to cause significant influence on the surface quality of finished product. Once the lubricant entraps in the surface features and its release is locked by the rolling/sliding roll or die, the internal fluid pressure not only resists elimination of surface features which effect the surface quality of finished product, but also if the fluid pressure

exceeds the yield strength of the material, it can cause further plastic deformation leading to poorer surface quality. In the current investigation the surface quality will be better for the re-HIPed alloy as the release of lubricant towards the trailing edge of contact region, with a moving slider or roller, will result in less severe surface damage due to higher nanoscale deformation resistance of the metal matrix phase of the re-HIPed alloy.

4.3.6   *Comparison with ASTM G-65 abrasive wear tests*

The improved nanoscale tribo-mechanical performance of re-HIPed Stellite 6 alloy in this investigation is consistent with previously reported macroscale abrasive dry sand rubber wheel (DSRW – ASTM G-65) tests, as shown in **Figure 15** [22, 23]. An improvement of almost 14% in abrasive wear volume of re-HIPed Stellite 6 alloy can be appreciated from the DSRW tests shown in Figure 15. This is consistent with the improvement in nanoscratch wear resistance of re-HIPed alloy in the current investigation. As the sand particles plough through the matrix in DSRW, the mechanism of wear is dominated by the properties of the metal matrix. The nanoscratch analysis in the current investigation therefore provides a basis for the mechanism of this improved performance in DSRW tests due to the differences in the properties of metal matrix between the re-HIPed and cast alloys.

4.4 *FEM analysis*

The FEM results provided further insights in to the wear behaviour and indicated that the depth of plastic zone under the indenter was maximum up to a depth of 8 µm (Figure 13) for a plastically deformed wear scar depth of 300nm (Figures 8c,d). This indicates that the plastic deformation seen at the edges of the wear tracks in the AFM images in Figures 8 and 9 is only indicative of the shallow tensile stress at the edge of the contact region. The plastic deformation and work-hardening depth is orders of magnitude higher than that observed at the edges of the wear track. Von Mises stress under the contact zone after nanoscratch tests was of the order of 350 MPa and indicates the level of stress residual after the removal of indenter. Of course it can be argued that during loading the stress will have both elastic and plastic components and hence will be much higher than 350 MPa. An estimation of the elastic to plastic work discussed earlier in section 4.3.3 indicates that the ratio of elastic recovery was in the range of 69% to 51% for the loading conditions considered in this investigation (Figure 14). Hence the total stress i.e. elastic and plastic during scratching will be higher than the plastic residual stress of 350 MPa after the scratch, making the total stress on yield closer to the values quoted in Table 2 of 700MPa to 750 MPa. The comparison of wear morphology was consistent with the experimental observations (Figure 12), which was reflected in the quantitative analysis of wear volume and its comparison with the experimental analysis. The average scratch volume loss from the experimental results (Figure 11) for the re-HIPed and cast Stellite 6 alloys compared well with the FEM results, and the percentage error ranged from 19% to 25% for the cast alloy, and 0% to 18% for the re-HIPed alloy. The FEM predictions of wear volume were closer to that of experimentally measured re-HIPed results due to the microstructural homogeneity and finer microstructure of the re-HIPed alloy.

5. CONCLUSIONS

1) Nanoscratch testing of re-HIPed and cast Stellite 6 alloys indicated differences in the wear behaviour at nanoscale between the metal matrix and carbide phases. The microstructural homogeneity and higher hardness of metal matrix phase in the re-HIPed alloy led to relatively lower volume loss in comparison to the cast counterpart.

2) In terms of the structure property relationships, the absence of tungsten rich carbides in the re-HIPed alloy indicated tungsten was retained in the metal matrix phase due to sluggish diffusion during re-HIPing. This provided more resistance to plastic deformation in the matrix phase of the re-HIPed alloy due to roughening of slip planes and decrease in stacking fault energy.

3) The metal matrix phase of the cast alloy in comparison to the re-HIPed counterpart indicated lower resistance to ploughing which was attributed to the lower hardness of the matrix phase. Shear bands were also observed in the cast alloy during nanoscratch testing indicating strain dependent transformation and a higher rate of work-hardening.

4) The strain rate during nanoscratch testing also had an influence on the wear rate for equal energy conditions. Loading condition 2 therefore resulted in higher wear volume loss in comparison to loading condition 3, which had same average energy during scratch testing.

5) Improved wear performance of re-HIPed alloy during nanoscratch testing in this investigation is consistent with dry rubber sand wheel abrasive wear tests.

6) The FEM analysis provided further insights on the calculation of plastically deformed zone under the contact region and wear volume displaced. There was good agreement between the wear volume loss values of the FEM and experimental analysis.

6. REFERENCES

[1] Crook, P., 1994, "Cobalt-base Alloys Resist Wear, Corrosion, and Heat," Adv. Alloys & Prog., 145(4), pp. 27-30.

[2] Antony, K. C., 1983, "Wear-resistant Cobalt-based Alloys," J. of Metals, 5(2), pp. 52-60.

[3] Frenk, A., and Kurz, W., 1994, "Microstructural Effects on the Sliding Wear Resistance of a Cobalt-based Alloy," Wear, 174, pp. 81-91.

[4] Berns, H., and Wendl, F., 1985, "Microstructure and Properties of CoCr29W (Stellite 6) in the As-cast, Forged and Powder Metallurgical Condition," Proceedings of Second International Conference on Cobalt, Venice, Italy, pp. 292-305.

[5] D.Klarstrom, P.Crook, J.Wu, 2004, "Metallography and Microstructures of Cobalt and Cobalt Alloys", ASM Handbook, ASM Handbook, Volume 9: Metallography and Microstructures, G.F. Vander Voort, editor, p762–774, DOI: 10.1361/asmhba0003771.

[6] Shin, J. C., Doh, J. M., Yoon, J. K., Lee, D. Y., and Kim, J. S., 2003, "Effect of Molybdenum on the Microstructure and Wear Resistance of Cobalt-base Stellite Hardfacing Alloys," Surf. and Coat. Tech., 166, pp. 117-126.

[7] Kuzucu, V., Ceylan, M., Celik, H., and Aksoy, I., 1998, "An Investigation of Stellite-6 Alloy Containing 5.0 wt% Silicon," J. of Alloys Pro. Tech., 79, pp. 47-51.

[8] Wang, L. C., and Li, D. Y., 2003, "Effects of Yttrium on Microstructure, Mechanical Properties and High-temperature Wear Behavior of Cast Stellite 6 Alloy," Wear, 255, pp. 535-544.

[9] De Mol van Otterloo, J. L., and De Hosson, J. T. M., 1997, "Microstructure and Abrasive Wear of Cobalt-based Laser Coatings, "Scripta Alloyia, 36, pp. 239-245.

[10] Crook, P., and Levy, A. V., 1992, "Friction and Wear of Cobalt-Base Wrought Alloys," ASM Handbook, Vol. 18, ASM Materials Park, OH, pp. 766-771.

[11] Klarstrom, D. L., 1993, "Wrought Cobalt-Base Superalloys," J. of Alloys Eng. and Perform., 2(4), pp. 523-530.

[12] Kim, H. J., and Kim, Y. J., 1999, "Wear and Corrosion Resistance of PTA Weld Surfaced Ni and Co Based Alloy Layers," Surf. Eng., 15(6), pp. 495-501.

[13] Silence, W. L., 1978, "Effect of Structure on Wear Resistance of Co-, Fe-, and Ni- Base Alloys," J. of Lubrication Technology, Transactions of the ASME, 100, pp. 428-435.

[14] Kosel, T. H., Li, S. Z., and Rao, C. M., 1985, "The Size Effect in Abrasion of Dual-Phase Alloys," ASLE Transactions, 28(3), pp. 343-350.

[15] Desai, V. M., Rao, C. M., Kosel, T. H., and Fiore, N. F., 1984, "Effect of Carbide Size on the Abrasion of Cobalt-Base Powder Metallurgy Alloys," Wear, 94, pp. 89-101.

[16] Yang, L. J., and Loh, N. L., 1995, "The Wear Properties of Plasma Transferred Arc Cladded Stellite Specimens," Surf. and Coat. Tech., 71, pp. 196-200.

[17] Cooper, D., Davis, F. A., and Wood, R. J. K., 1992, "Selection of Wear-Resistant Alloys for the Petrochemical Industry," J. of Phys. D: Applied Physics, 25, pp. A195-A204.

[18] Song, J. H., and Kim, H. J., 1997, "Sliding Wear Performance of Cobalt-Based Alloys in Molten-Al-added Zinc Bath," Wear, 210, pp. 291-298.

[19] De Mol van Otterloo, J. L., and De Hosson, J. T. M., 1997, "Microstructural Features and Mechanical Properties of a Cobalt-based Laser Coating," Acta Materialia, 45, pp. 1225-1236.

[20] Yu, H., Ahmed, R., and De Villiers Lovelock, H., 2007, "A Comparison of the Tribo-mechanical Properties of wear-resistant cobalt-based alloys produced by different manufacturing processes," ASME J. of Tribol., 129, pp. 586-594.

[21] Kumar, P., 1986, "Properties in P/M Stellite Alloy No. 6," Progress in Powder Metallurgy, 41, pp. 415-437.

[22] Ahmed, R., de Villiers Lovelock, H., Davies, S., Faisal, N. H., 2013, "Influence of re-HIPing on the structure property relationships of cobalt-based alloys", Tribology International, Vol. 57, pp. 8-21.

[23] Yu, H., Ahmed, R., de Villiers Lovelock, H., and Davies, S., 2009, "Influence of Manufacturing Process and Alloying Element Content on the Tribomechanical Properties of Cobalt-Based Alloys", ASME Journal of Tribology, Vol. 131(1), pp. 11601-11613, doi:10.1115/1.2991122.

[24] Stoica, V., Ahmed, R., and Itsukaichi, T., 2005, "Influence of Heat Treatment on the Sliding Wear of Thermal Spray Cermet Coatings", Surface and Coatings Technology, Vol. 199(1), pp. 7-21.

[25] Stoica, V., Ahmed, R., Itsukaichi, T., and Tobe, S., 2004, "Sliding Wear Evaluation of HIPed Thermal Spray Cermet Coatings", Wear, Vol. 257 (11), pp. 1103-1124.

[26] Sebastiani, M., Mangione, V., De-Felicis, D., Bemporad, E., Carassiti, F., 2012, "Wear mechanisms and in-service surface modifications of a Stellite 6B Co-Cr alloy", Wear, 290-291, pp. 10-17.

[27] Yao, M. X., Wu, J. B. C., Xie, Y., 2005, "Wear, corrosion and cracking resistance of some W- or Mo-containing Stellite hardfacing alloys", Material Science and Engineering A, 407, pp. 234-244.

[28] Oliver W. C., Pharr G. M., 1992, "An improved technique for determining hardness and elastic modulus using load and displacement sensing indentation experiments", J Mater Res 7:1564-83.

[29] Ashraf, M. A., Sobhi-Najafabadi, B., Göl, Ö., and Sigimar, D. 2007 'Numerical simulation of sliding wear for a polymer–polymer sliding contact in an automotive application', International Journal of Advanced Manufacturing Technology, DOI 10.1007/s00170-008-1560-z.

[30] Li, J., & Beres, W. (2007). Scratch test for coating/substrate systems–A literature review. Canadian Metallurgical Quarterly, 46(2), 155-173.

[31] Ahmed, R., Fu, Y. Q., Faisal, N. H., 2012, "Fatigue at nanoscale: an integrated stiffness and depth sensing approach to investigate the mechanisms of failure in DLC film, ASME Journal of Tribology, Vol. 134(1), pp. 012001-012009, http://dx.doi.org/10.1115/1.4005774.

[32] Jeng, Y. R., Tsai, P. C., Chiang, S. H., 2013, "Effects of grain size and orientation on mechanical and tribological characterizations of nanocrystalline nickel films", Wear, 303, pp. 262-268.

[33] Kim, H. H., Cho, S. H., Kang, C. G., "Evaluation of microstructure and mechanical properties by using nano/micro-indentation and nanoscratch during aging treatment of rheo-forged Al 6061 alloy", Material Science and Engineering A, 485, pp. 272-281, 2008.

[34] Hodge, A. M., Nieh, T. G., "Evaluating abrasive wear of amorphous alloys using nanoscratch technique", Intermetallics, 12, pp. 741-748, 2004.

[35] Huang, Y., Chiu, Y. L., Shen, J., Sun, Y., Chen, J.J., "Mechanical performance of metallic glasses during nanoscratch tests", Intermetallics, 18, pp. 1056-1061, 2010.

[36] Persson, D. H., Coronel, E., Jacobson, S., 2006, "Surface analysis of laser cladded Stellite exposed to self-mated high load dry sliding", Wear, 261(1), 96–100.

[37] Ahmed, R., and Sutcliffe, M. P. F., 2000, "Identification of surface features on cold rolled stainless steel strip", Wear, Vol. 244, pp. 60-70.

[38] Ahmed, R., and Sutcliffe, M. P. F., 2001, "An Experimental investigation of surface pit evolution during cold rolling or drawing of stainless steel strip", ASME, Journal of Tribology, Vol. 123, pp. 1-7.
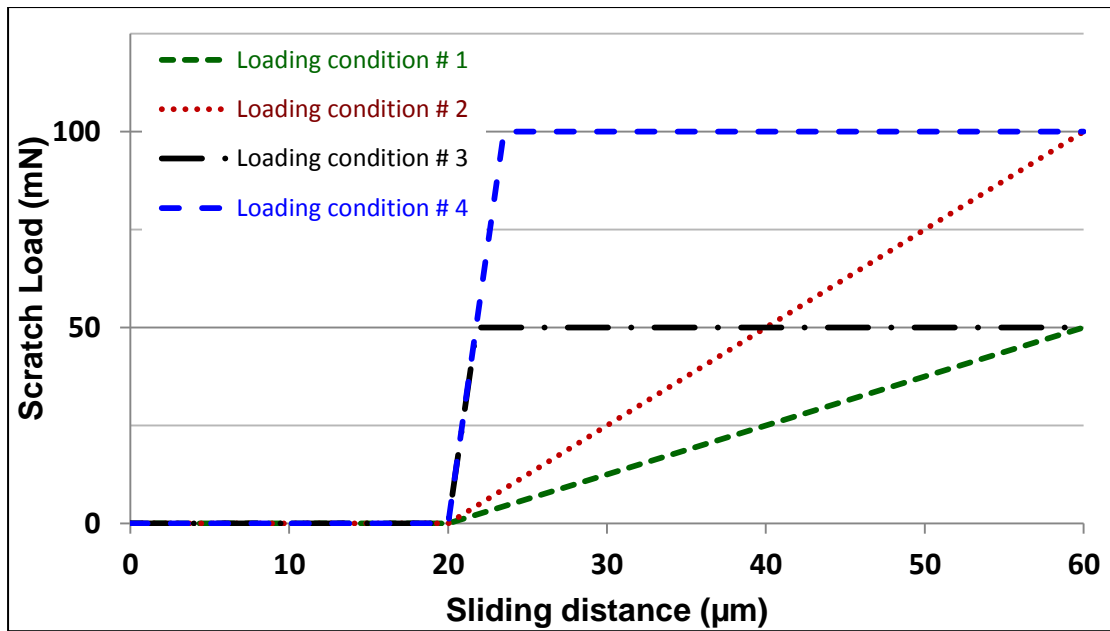
Figure 1, Loading conditions used for scratch testing. Load was ramped linearly after 20 μm travel at 2.5 mN/s to reach 50 mN and at 5 mN/s to reach 100 mN for loading conditions 1 (1 μJ) and 2 (2 μJ), respectively. For the loading conditions 3 (2 μJ) and 4 (3.83 μJ), the load was increased linearly after 20 μm travel at 25 mN/s to reach 50 mN and at 50 mN/s to reach 100 mN, respectively.
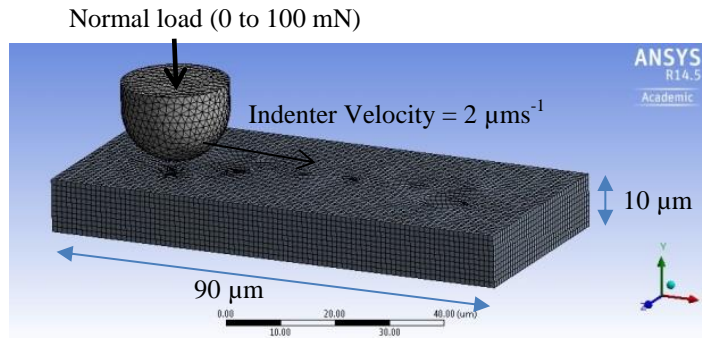
Normal load (0 to 100 mN)

Indenter Velocity = 2 µms⁻¹

ANSYS
R14.5
Academic

10 µm

90 µm

0.00   20.00   40.00 (um)
        10.00   30.00

Figure 2, Finite element model (FEM) geometry of scratch test.

(a)

20 µm

(b)

200 µm

(c)

Cr-rich
carbides

W-rich
carbides

Co-rich
matrix

Acc.V Spot Magn   Det WD   20 µm
20.0 kV 4.6 1600x   BSE 10.0 Heriot-Watt

(d)

Cr-rich
carbides

Co-rich
matrix

Acc.V Spot Magn   Det WD   10 µm
20.0 kV 5.2 3200x   BSE 10.0 0.5 Torr
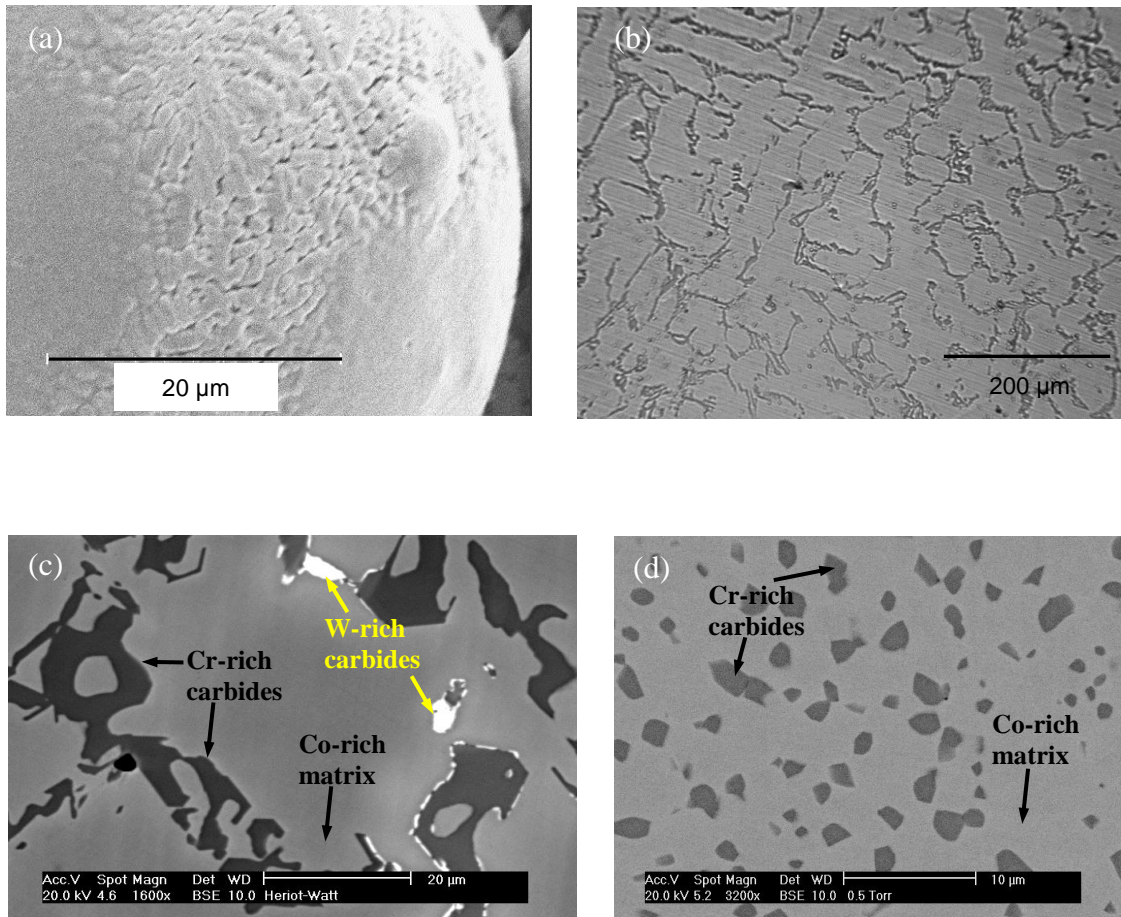
Figure 3, The images showing (a) the morphology of alloy powder; the microstructure of (b) and (c) cast Stellite 6 alloy; (d) re-HIPed Stellite 6 alloy.
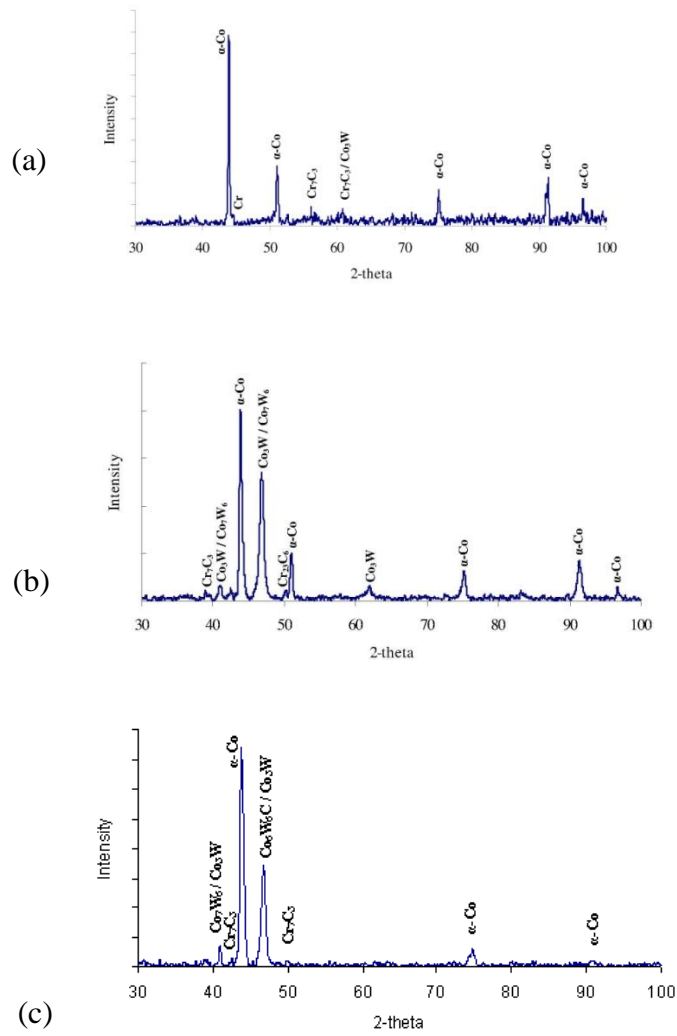
Figure 4, The XRD pattern of (a) alloy powder; (b) re-HIPed Stellite 6 alloy; (c) cast Stellite 6 alloy.
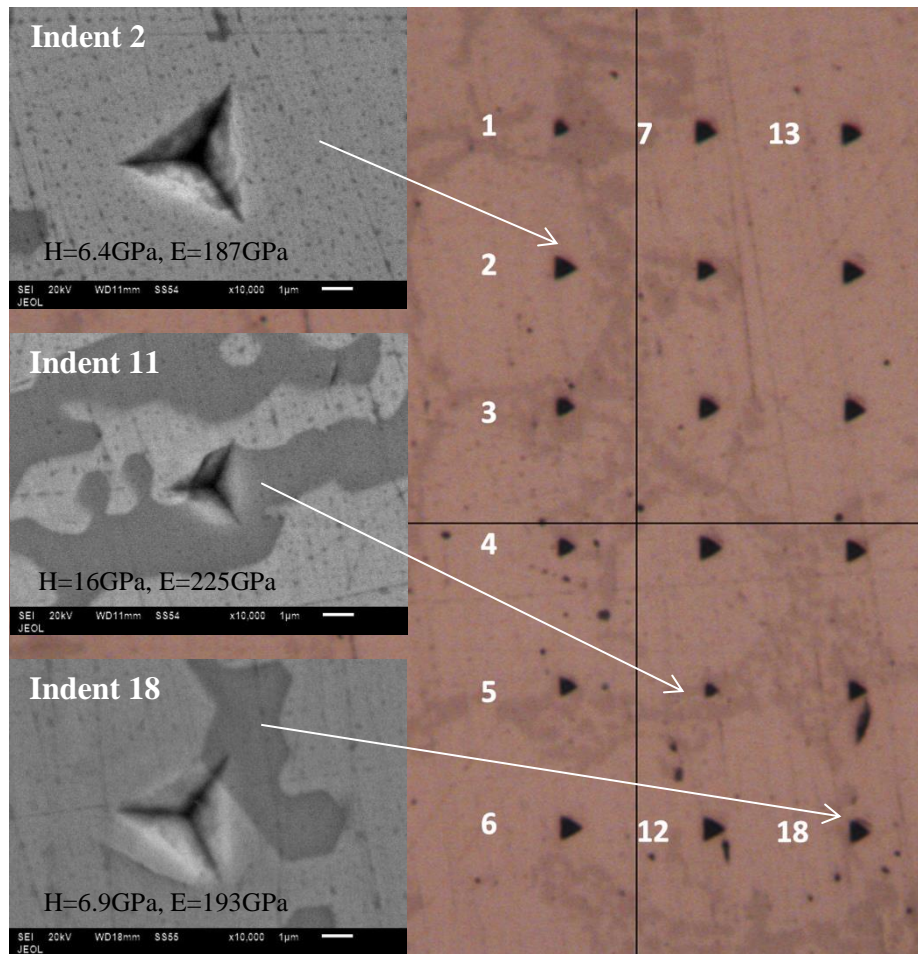
Figure 5, SEM and light microscope observations of the nanoindentations on the cast alloy.
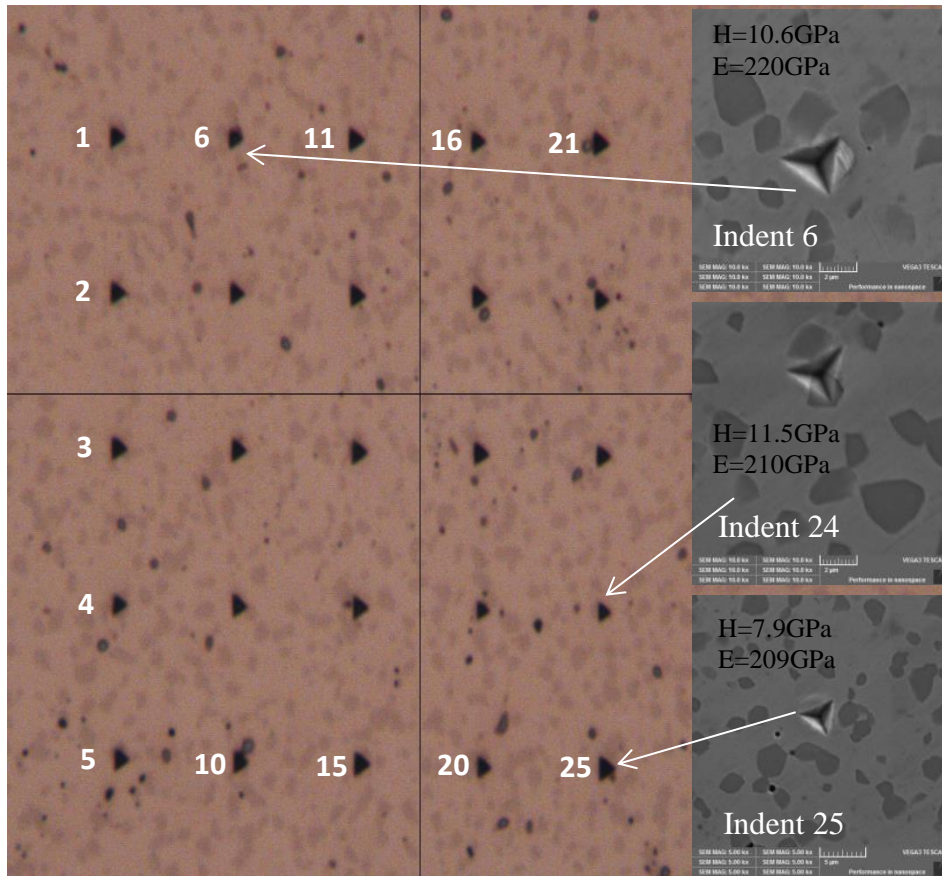
Figure 6, SEM and light microscope observations of the nanoindentations on the re-HIPed alloy.
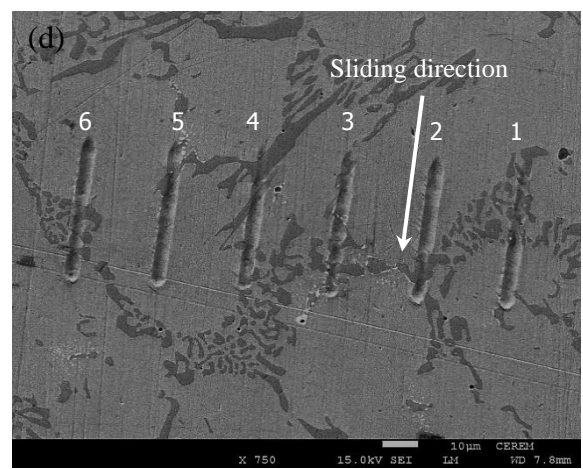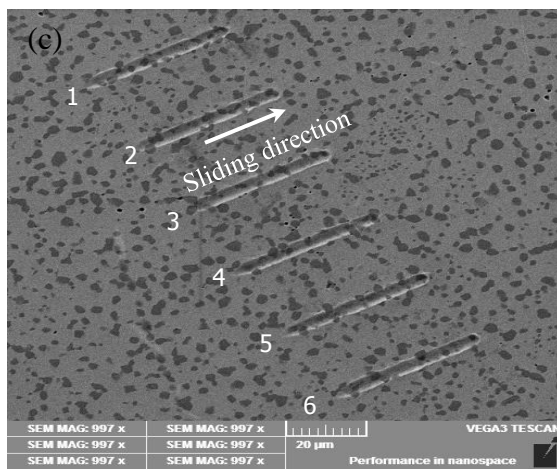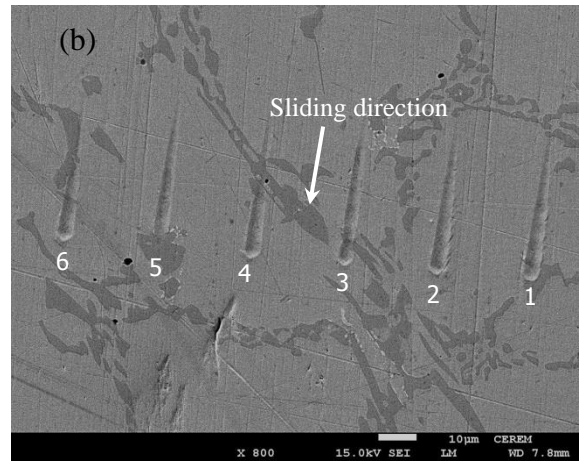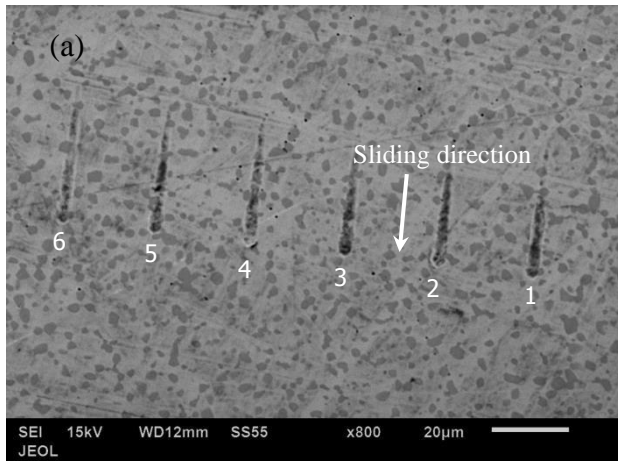
Figure 7, Scratches 1-6 as seen under SEM for loading conditions 1 and 3; (a) re-HIPed Stellite 6 at 50mN load; (b) cast Stellite 6 at 50mN load; (c) re-HIPed Stellite 6 at 50mN load; (d) cast Stellite 6 at 50mN load.
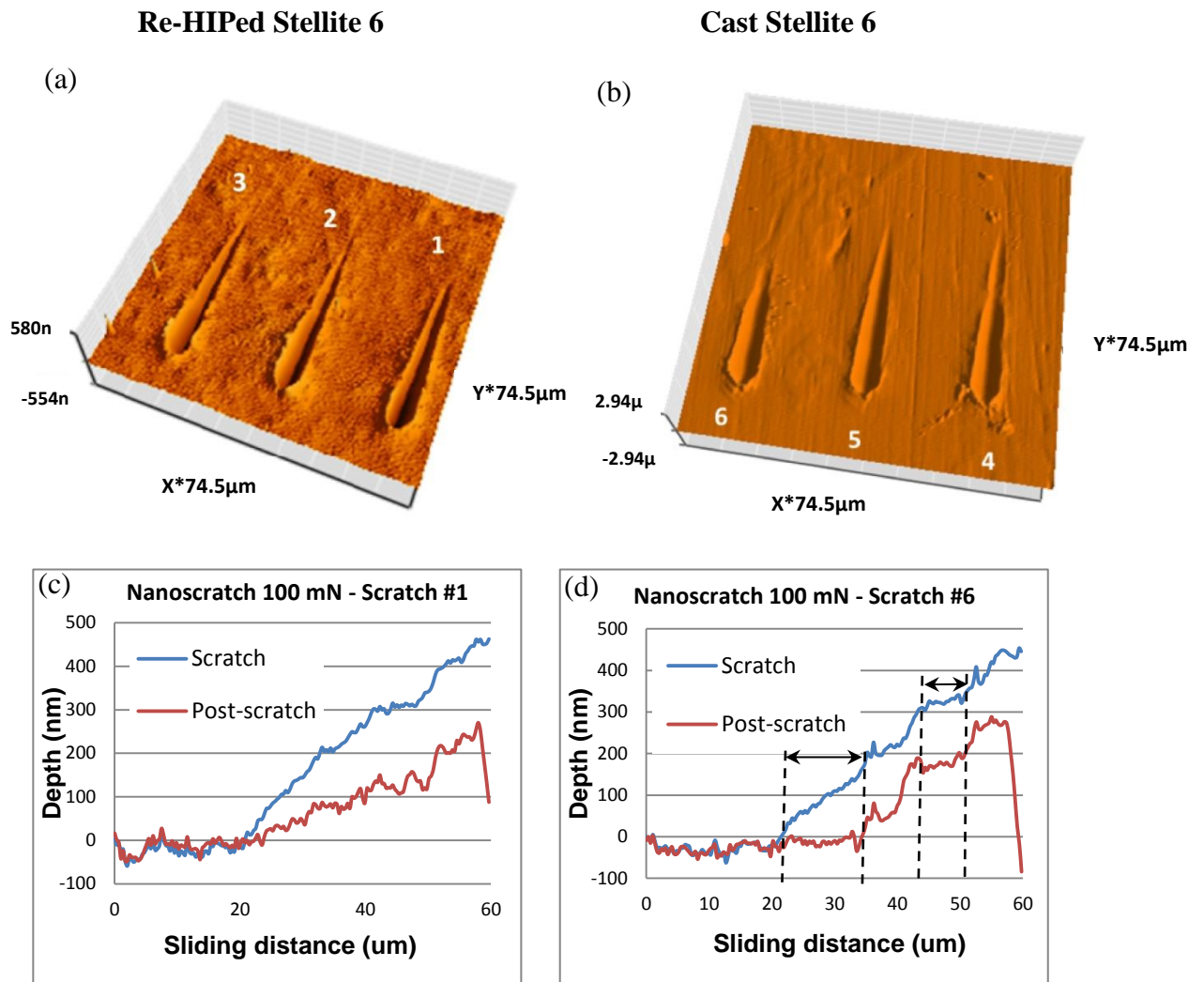
Figure 8, Comparison of scratch morphology between re-HIPed and cast Stellite 6 alloys at 100mN load for loading conditions 2; (a) topography map of scratches 1, 2 and 3 for re-HIPed Stellite 6; (b) topography map of scratches 4, 5 and 6 for cast Stellite 6; (c,d) pre and post-scan depth profile of wear scar 1 and 6 for re-HIPed and cast Stellite 6 alloys, respectively; (e,g) SEM observations of wear scar 1 for re-HIPed Stellite 6 alloy; (f,h) SEM observations of wear scar 6 for cast Stellite 6 alloy. Figure 8 continued overleaf.
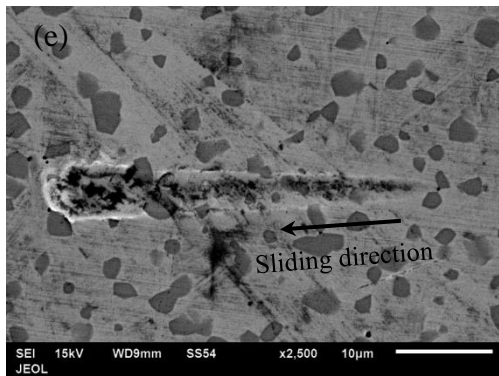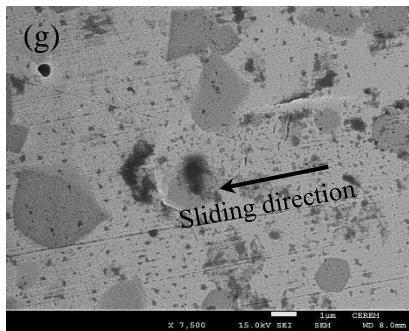
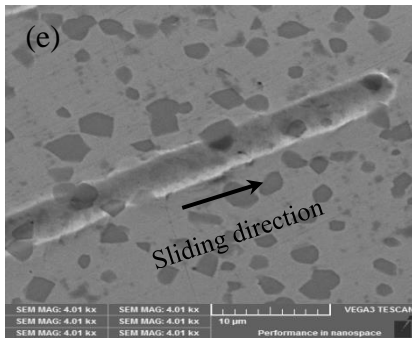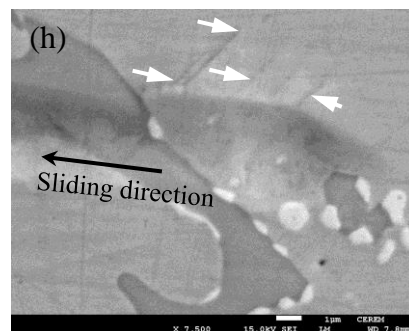**Re-HIPed Stellite 6**   **Cast Stellite 6**
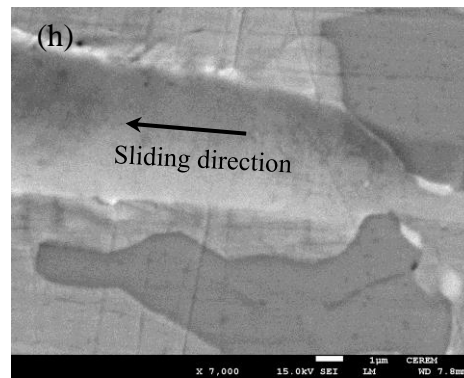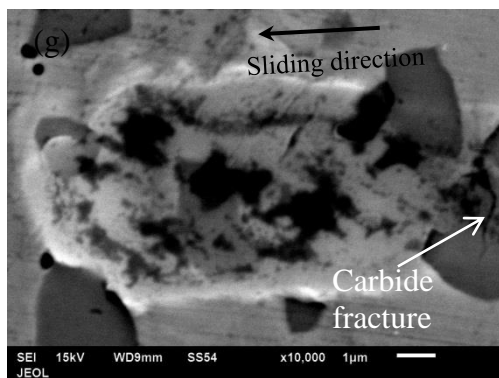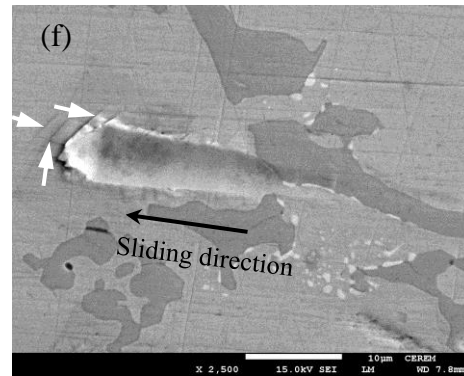
Continued Figure 8, Comparison of scratch morphology between re-HIPed and cast Stellite 6 alloys at100mN load for loading conditions 2; (a) topography map of scratches 1, 2 and 3 for re-HIPed Stellite 6; (b) topography map of scratches 4, 5 and 6 for cast Stellite 6; (c,d) pre and post-scan depth profile of wear scar 1 and 6 for re-HIPed and cast Stellite 6 alloys, respectively; (e,g) SEM observations of wear scar 1 for re-HIPed Stellite 6 alloy; (f,h) SEM observations of wear scar 6 for cast Stellite 6 alloy. White arrows in Figure 8(f) indicate the location of shear bands.
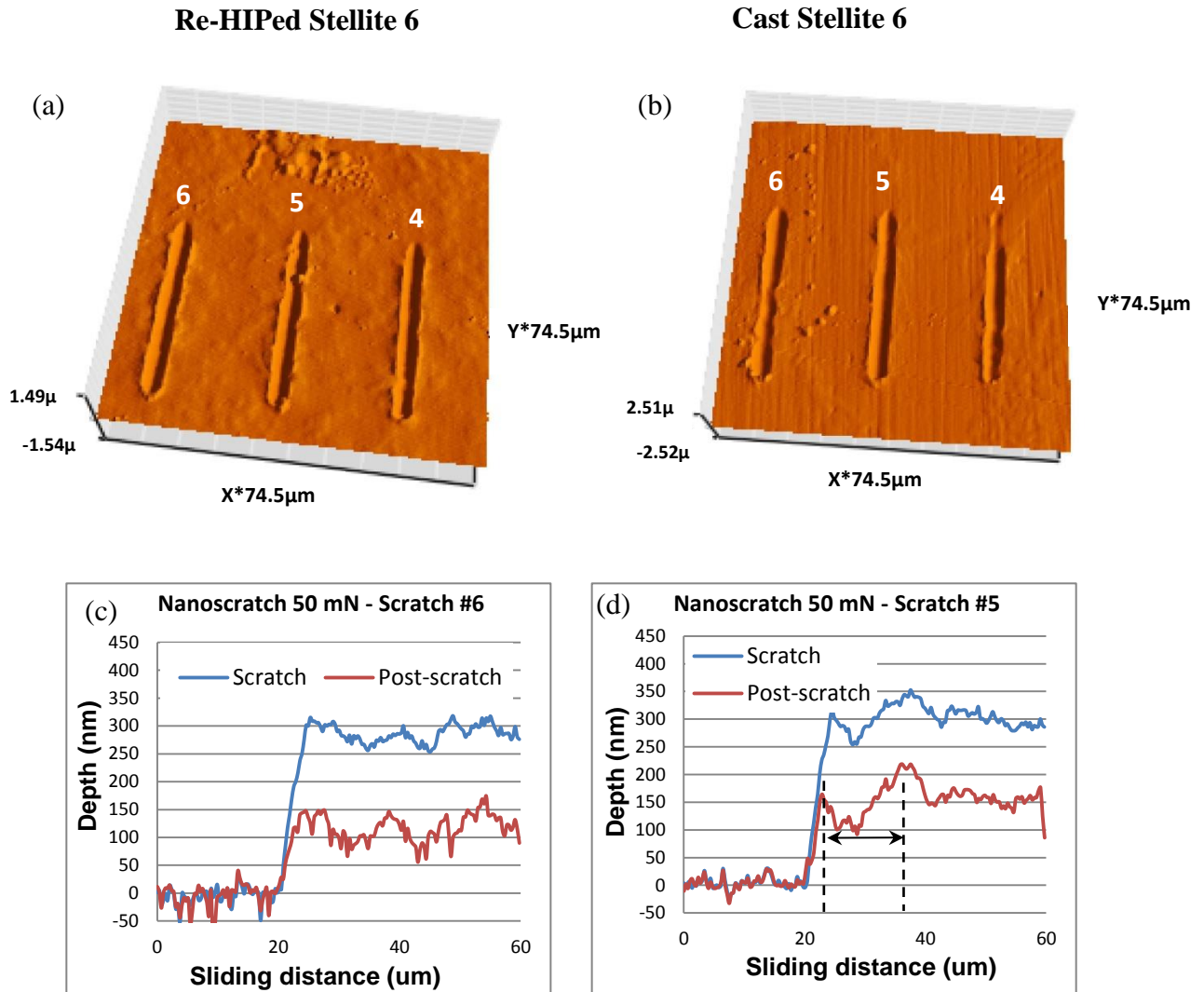
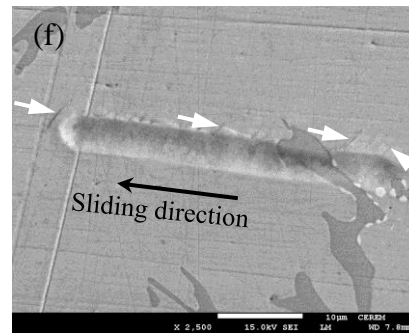**Re-HIPed Stellite 6**   **Cast Stellite 6**

Figure 9, Comparison of scratch morphology between re-HIPed and cast Stellite 6 alloys for loading conditions 3 at 50mN; (a) topography map of scratches 4, 5 and 6 for re-HIPed Stellite 6; (b) topography map of scratches 4, 5 and 6 for cast Stellite 6; (c,d) pre and post-scan depth profile of wear scar 6 and 5 for re-HIPed and cast Stellite 6 alloys, respectively; (e,g) SEM observations of wear scar 6 for re-HIPed Stellite 6 alloy; (f,h) SEM observations of wear scar 5 for cast Stellite 6 alloy. <mark>Figure 9 continued overleaf.</mark>

Re-HIPed Stellite 6   **Cast Stellite 6**

Continued Figure 9, Comparison of scratch morphology between re-HIPed and cast Stellite 6 alloys for loading conditions 3 at 50mN; (a) topography map of scratches 4, 5 and 6 for re-HIPed Stellite 6; (b) topography map of scratches 4, 5 and 6 for cast Stellite 6; (c,d) pre and post-scan depth profile of wear scar 6 and 5 for re-HIPed and cast Stellite 6 alloys, respectively; (e,g) SEM observations of wear scar 6 for re-HIPed Stellite 6 alloy; (f,h) SEM observations of wear scar 5 for cast Stellite 6 alloy. White arrows in Figure 9(f, h) indicate the location of shear bands.
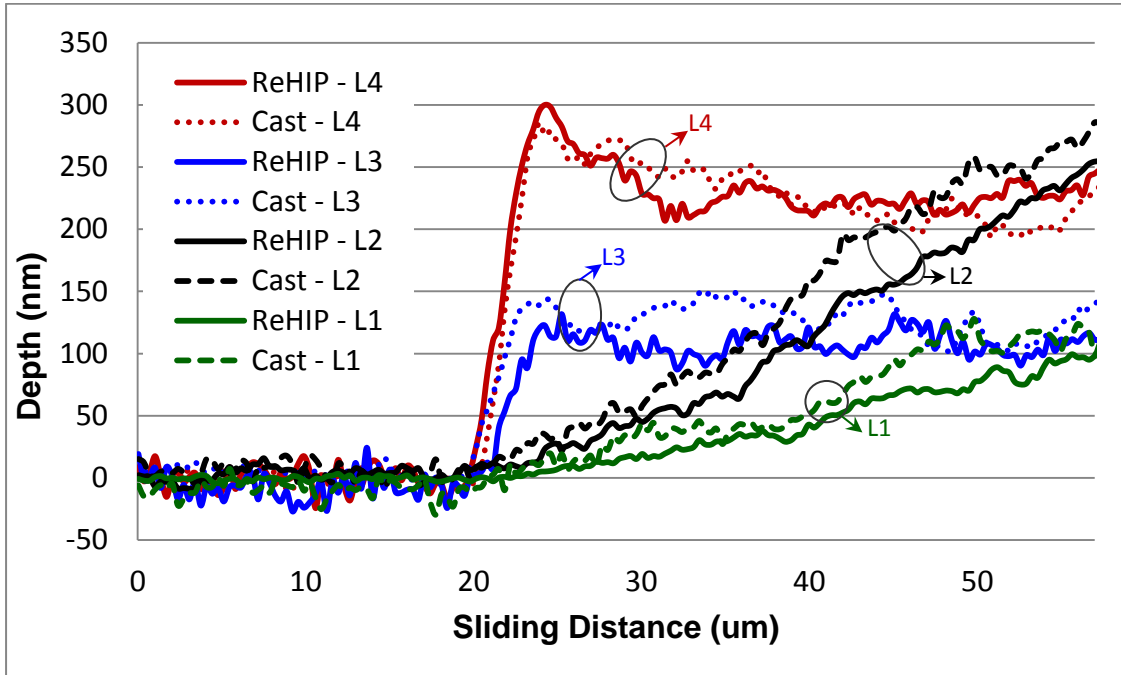
Figure 10, Averaged wear scar depths along the nanoscratch direction for all loading cases. L1, L2, L3 and L4 represent loading conditions 1 to 4, respectively. The sold lines represent the re-HIPed alloy whereas the dotted lines indicate the averaged profiles of the cast alloy.
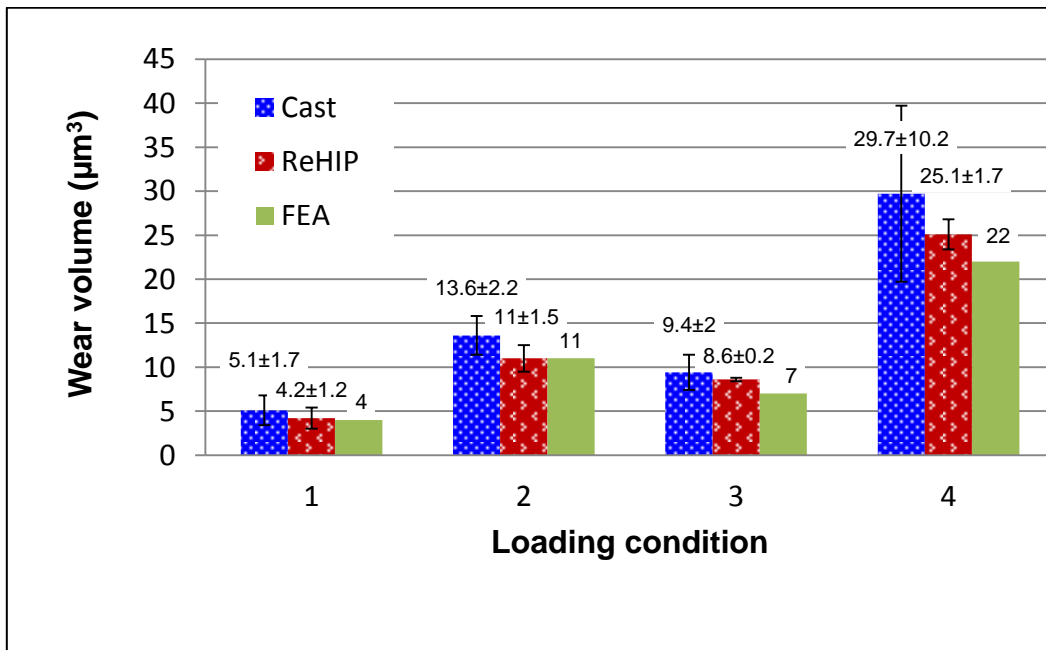

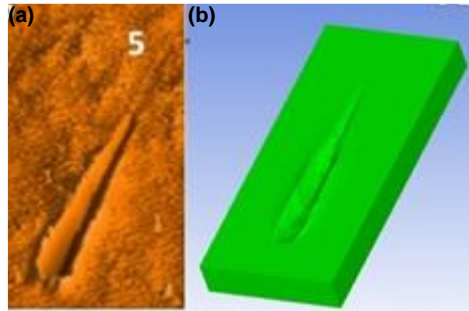Figure 11, Average wear volume for loading conditions 1 to 4.

Figure 12, Comparison of post nanoscratch test observations at 100 mN load for loading condition 2; (a) AFM surface topography of scratch 5; (b) FEM output from ANSYS.
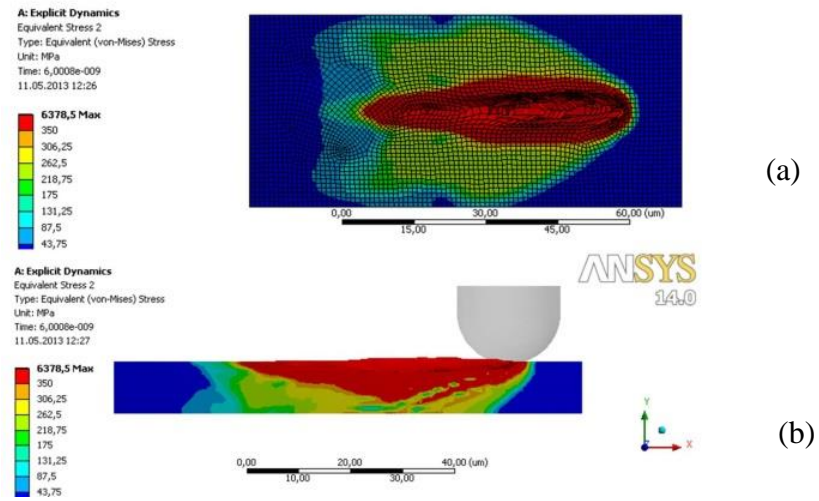

Figure 13, FEM results of nanoscratch test: Von Mises stress distribution for 60 micron length at 100 mN load (Loading condition 2); (a) along the thickness (y-axis); (b) laterally along (z-x axis).
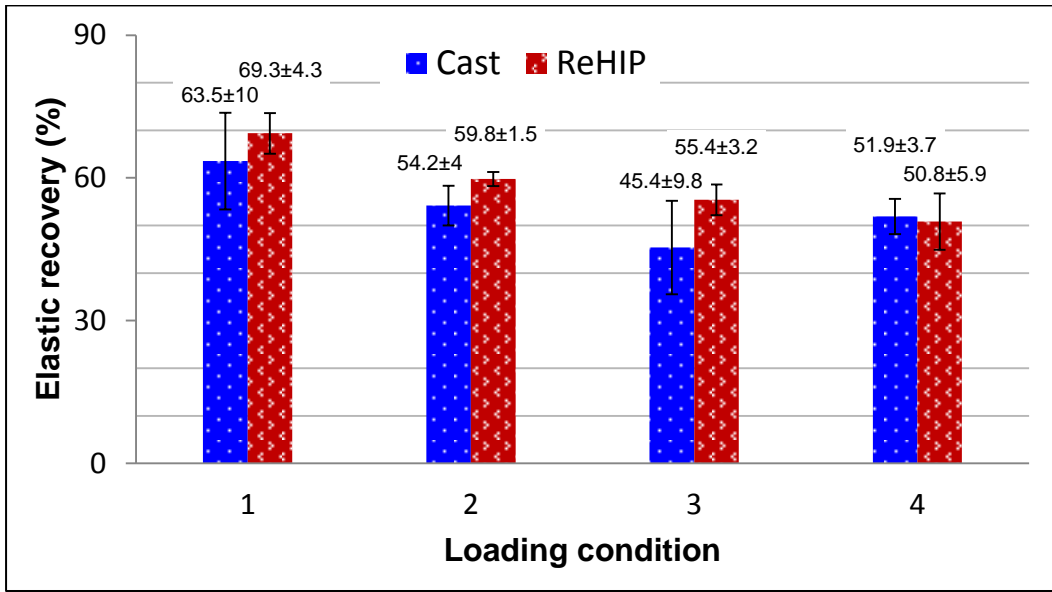
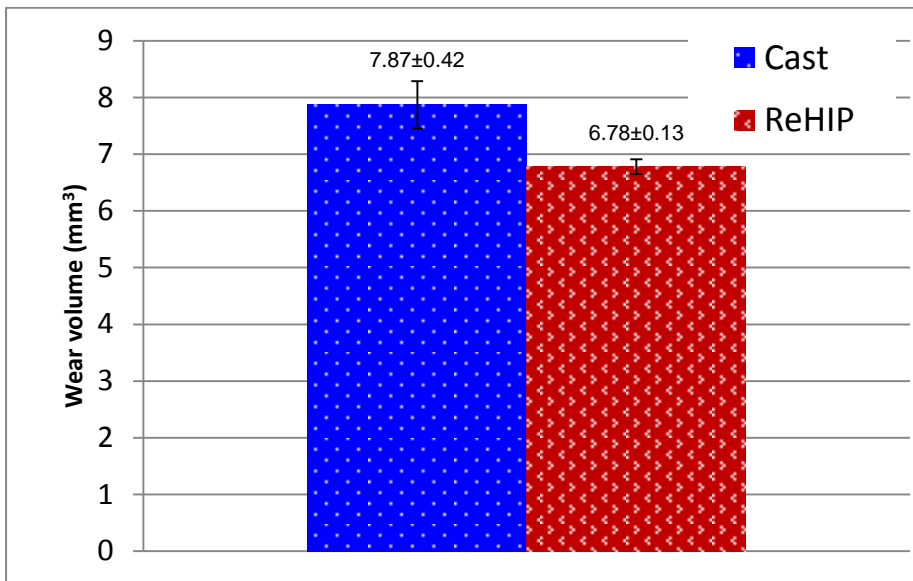Figure 14, Elastic recovery of Stellite 6 alloys after scratch tests.

Figure 15, Dry rubber sand wheel (DRSW) abrasion test results of cast and re-HIPed Stellite 6 alloys according to ASTM G65-04 [22,23].

Table 1
The chemical compositions of cast and re-HIPed Stellite 6 alloys (wt. %).

	Co	Cr	W	C	Mo	Fe	Ni	Mn	Si
Cast Stellite 6 alloy	Bal.	27.10	4.95	0.95	0.30	1.10	0.60	0.90	1.24
re-HIPed Stellite 6 alloy	Bal.	29.50	4.60	1.09	0.22	2.09	2.45	0.27	1.32

Table 2
Material parameters used in finite element analysis.

	Re-HIPed Stellite 6	Cast Stellite 6
Elastic modulus (GPa)	237	209
Yield strength (MPa)	750	700
Ultimate tensile strength (MPa)	1265	850
Elongation (%)	4	1
Density (kg/m^3)	8440	8440

Table 3
The volume fraction of individual phases in cast and re-HIPed Stellite 6 alloys.

	Cr-rich carbides (Dark phase)	W-rich carbides (Bright phase)	Co-rich matrix (Grey region)
Cast Stellite 6 alloy	14.5 ± 6.6%	1.0 ± 0.5%	84.5 ± 7.0%
re-HIPed Stellite 6 alloy	15.0 ± 0.7%	0.0%	85.0 ± 0.7%

Table 4
Average, maximum and minimum values in GPa of nanohardness and modulus in re-HIPed and cast Stellite 6 alloys.

	re-HIPed Stellite 6	Cast Stellite 6
Average nanohardness	9.1 ± 0.96	8.5 ± 2.86
Maximum hardness relating to Carbide (GPa)	11.5 ˜ 10.5	16 ˜ 14.97
Minimum hardness relating to matrix (GPa)	7.4 ˜ 7.9	6.4 ˜ 6.9
Average modulus (GPa)	210.9 ± 5	203.2 ± 14
Maximum modulus (E_r) relating to carbide (GPa)	220 ˜ 214	243 ˜ 225
Minimum modulus (E_r) relating to matrix (GPa)	200 ˜ 206	187 ˜ 194
Microhardness ($HV_{2.94N}$) [22,23]	459.3 ± 10.4	402.6 ± 20.9
Macrohardness (HV_{294N}) [22,23]	403 ± 2.6	408 ± 3.8